Quiescent Regions Below the X-Point in ASDEX Upgrade

R. D. Nem[1], P. Manz[2], J. Juul Rasmussen[1], N. Vianello[3], N. Walkden[4], V. Naulin[1], B. Sieglin[2], A. Herrmann[2], D. Brida[2] and the ASDEX Upgrade Team[2,5]

[1]Technical University of Denmark, Kgs. Lyngby, Denmark
[2]Max Planck Institute for Plasma Physics, Boltzmannstr. 2, 85748 Garching, Germany
[3]Consorzio RFX, Padua, Italy
[4]CCFE, Culham Science Centre, Abington, OX14 3DB, United Kingdom
[5] H. Meyer et al. 2019 Nucl. Fusion 59 112014

E-mail: nishta@fysik.dtu.dk

Abstract. Probe measurements of plasma fluctuations in the divertor region of ASDEX Upgrade reveal the existence of *two* quiescent regions close to the separatrix: one on the low field side scrape-off layer and one on the high field side of the private flux region. The X-point manipulator at ASDEX Upgrade provides the unique possibility of obtaining continuous measurements of the ion-saturation current from the low field side scrape-off layer through the private flux region and into the high field side scrape-off layer.

Keywords: X-point region, quiescent regions, private flux region, fluctuations, ASDEX Upgrade tokamak, Divertor region, X-point manipulator

1. Introduction

In tokamaks with a divertor configuration, plasmas are categorised into three regions: the core, the scrape-off layer (SOL) and the private flux region (PFR). The core is the region where the plasma is confined by magnetic field lines. The SOL is characterised by the flow of plasma along the 'open' magnetic field lines towards the plasma facing components (PFCs). The PFR is located below the X-point and is geometrically restricted by the two legs formed by the separatrix. The PFR is also characterized by 'open' magnetic field lines. At the upstream SOL, the cross-field transport has been identified as being non-diffusive [1, 2]. Non-diffusive turbulent transport is associated with filamentary structures also termed 'plasma blobs'. As a result of interchange turbulence, the filaments emerge from the low field side (LFS) edge of the plasma and subsequently propagate into the SOL [3]. Measurements have shown that the filament

properties change with density [4]. At high density, a regime of increased filamentary transport leads to a shoulder formation [4,5]. The shoulder formation is an active field of research, since ITER and DEMO will be operated at high densities and will feature detached divertors [4]. The filamentary transport also influences the ratios of parallel to perpendicular particle and heat fluxes [6]. This determines the confinement of the plasma and the power-deposition area on the PFCs, which in turn, has a significant impact on the lifetime of the PFCs [7]. To be able to quantify the erosion of the PFC material, statistics of the plasma fluxes to the PFCs and measurements of the fluctuating quantities in the SOL turbulence are important. Whilst significant progress has been made towards a comprehensive understanding of SOL physics, some knowledge are still missing due to a lack of measurements around the X-point.

The presence of the X-point influences the filamentary structures and the turbulence in the SOL making it a crucial region to investigate. Strong magnetic shearing near the X-point causes the flux tubes to shear into ribbon like structures [8]. Strongly elongated structures as the plasma filaments observed upstream cannot exist close to the X-point [8,9]. This results in a quiescent region on the LFS SOL. The presence of a quiescent region was first reported for MAST by Walkden et al. [12], where L-mode data taken with a high speed visible imaging camera showed fewer filaments in the vicinity of the X-point in the LFS SOL. Measurements in MAST, NSTX and TCV show a quiescent region close to the X-point in the SOL in lower single null L-mode discharges [12–15]. The quiescent region in the LFS SOL has also been seen in simulations carried out using the 3D fluid turbulence code TOKAM3X [16–18].

Furthermore, the strong shearing around the X-point can lead to a disconnection of the turbulence upstream and downstream the X-point, thus the turbulence in the main chamber SOL can be decoupled from the turbulence close to the targets in the divertor region [10–12].

The X-point manipulator (XPM) at ASDEX Upgrade gives the unique poloidal diagnostics coverage and allows local measurements in the X-point region. In this paper, we present experimental data in the X-point region of ASDEX Upgrade tokamak to investigate the fluctuation amplitudes. Therefore, measurements through both the LFS and high field side (HFS) SOL as well as in the PFR are considered. Spectral analysis indicates the presence of a region of low fluctuation on the LFS SOL, similar to the quiescent region observed in MAST, and the presence of a second region of low fluctuation in the PFR that has not been reported before. This paper is structured as follows: the experimental setup is briefly described and the experimental details of the discharges are given in section 2. Section 3 introduces the methodological approach. In section 4, the results obtained from Langmuir probes mounted on the XPM are presented. The latter are discussed in section 5.

2. Diagnostic and experimental details

The divertor region of the poloidal cross-section of ASDEX Upgrade is shown in Fig. 1 (a). The XPM trajectory, represented by the black line, is located at $z = -0.965$ m in sector 10 of ASDEX Upgrade. The XPM reciprocates horizontally through the divertor entrance, starting from the LFS wall at a major radius of $R_m = 1.645$ m with a maximum insertion distance of $R_m = 1.356$ m on the HFS. For a typical magnetic equilibrium configuration the XPM moves just below the X-point. More information on the XPM can be found in [19–21]. A full probe plunge covers approximately 30 cm in the vacuum vessel allowing measurements in both the LFS- and the HFS SOL, as well as in the intermediate PFR. A maximum of three plunges are performed per plasma discharge to avoid overheating of the probe head. The probe head consists of three cylindrical Langmuir probe pins. Two of which are in a Mach configuration (pin 1 and pin 2) and one freestanding (pin 3). The latter is swept at a frequency of 1 kHz between approximately $\pm$ 130 V to measure current-voltage (I-V) characteristic curves. The probe head configuration and the direction of the toroidal magnetic field are shown in Fig. 1 (b). The Langmuir probe pins are approximately 2 mm long with a diameter of 1 mm. The area A of the pins are $\approx 6.6 \times 10^{-6}\mathrm{m}^2$. The graphite wall is 4 mm high and 0.9 mm wide. The distances between the pins and the center of the wall are denoted by x and y, where $x = 1.2$ mm and $y = 2.6$ mm.

We consider three different L-mode plasmas in a lower single null configuration. The presented set of discharges is limited to low power and low density discharges, because only under these conditions the heat towards the probe allowed for measurements. Nevertheless, these conditions allow the study of the effects of the divertor topology on fluctuation levels, which is currently of great interest as we want to improve the power exhaust. It should be noted that the divertor topology is the same for all the plasma discharges discussed in this work. The details of the discharges are listed in Tab. 1. Shot #35466 is a deuterium (D) plasma with electron-cyclotron-resonance heating (ECRH). Shots #36736 and #36744 are helium (He) plasmas with ECRH and neutral-beam injection (NBI) heating, respectively. The ion-saturation current is measured and applied as an approximation for the electron density fluctuation. However, frequent voltage break-in of the power supply has been observed during the experiments.

When the voltage break-in occurs, one cannot make the assumption of a dominant density fluctuation compared to the electron temperature fluctuation. Thus, many of the collected data had to be neglected and the most reliable discharges are presented in this work.

3. Data analysis

The time trace of the ion-saturation current I_{sat}^{+}, from the first plunge of the He plasma (#36744) is shown in Fig. 2 (a). It exhibits three stationary measurements of 20 ms in the insertion phase in each of the three regions below the X-point, namely the LFS

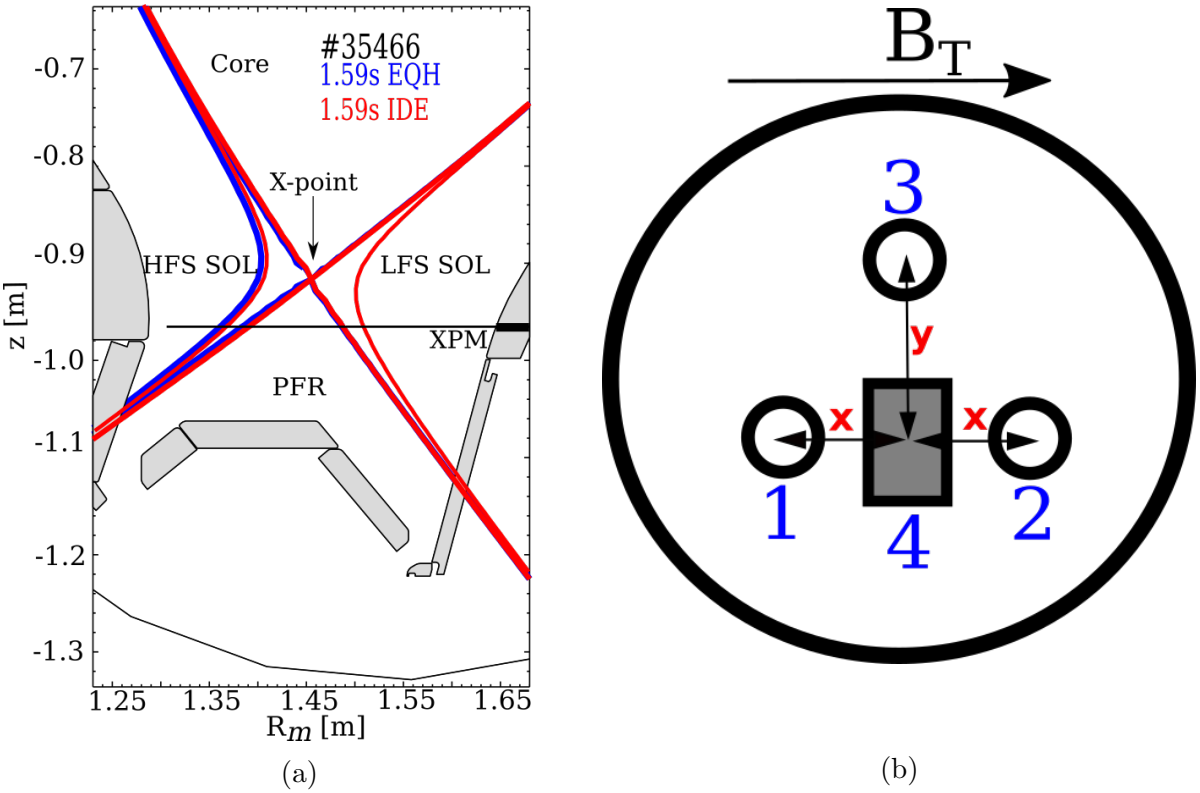

(a) (b)

Figure 1: (a) The divertor poloidal cross-section of ASDEX Upgrade together with the magnetic equilibrium-configuration of discharge #35466 and (b) the mounted configuration of the probe head and the direction of the toroidal magnetic field B_T. Pin 1 and 2 are in Mach configuration, while pin 3 is swept and 4 represents a graphite wall. The front head of the probe is 10 mm wide. $x = 1.2$ mm and $y = 2.6$ mm. Figure taken from [22].

SOL, PFR and the HFS SOL. The stationary phases can be identified by the plateaus in the XPM trajectory (shown in green). The PFR region is determined from equilibrium reconstruction. Only the insertion phase of the probe head is considered. During the retraction phase arcing is often observed making the data unsuitable for analysis. In Fig. 2 (b), the data of the three discharges used for the analysis are shown as a function of major radius R_m.

Since the measuring location is close to the X-point, it is challenging to numerically reconstruct the exact magnetic equilibrium of the private flux region for the measurements. Therefore, the private flux region is determined in three steps. First, the private flux region has been determined by comparing two magnetic equilibrium reconstruction codes used at ASDEX Upgrade (IDE [23] and EQH [24]). Fig. 1 (a) shows the magnetic reconstruction of the D discharge #35466 at time 1.59 s. The magnetic equilibrium using IDE code is shown in red colour and the EQH is in blue. The LFS separatrix legs are in good agreement for both codes, while for the HFS separatrix leg a difference of approximately 3 mm is observed. The EQH code gives a slightly broader

Shot #	Gas	B_T [T]	$\overline{n}_\mathrm{e}[10^{19}\mathrm{m}^{-3}]$	I_p [MA]	Power [MW]	Source
35466	D	-2.56	3.75	1.0	0.410	ECRH
36736	He	-2.56	3.13	1.0	0.444	ECRH
36744	He	-2.56	3.10	1.0	0.444	NBI

Table 1: L-mode, medium density discharges in a lower single null configuration used in this work. The table gives an overview of the fuelling gas used, the magnetic field strength B_T, the averaged-density $\overline{n}_\mathrm{e}$, the plasma current I_p, the power and lastly the type of auxiliary heating used [22].

PFR compared to the IDE code. From the magnetic reconstruction, the accuracy of determining the LFS separatrix leg is about ± 5 mm while for the HFS separatrix leg, it is approximately ± 1 cm.

As a second step, the determined PFR (using the codes from step one) is verified by plotting it on top of the measured ion-saturation current along the probe trajectory. The measurements have shown that the ion-saturation current decreases when moving from the LFS SOL into the PFR and it increases again when moving out of the PFR into the HFS, i.e., when crossing the separatrix leg. An example of the changes in the ion-saturation current in the three regions is shown in fig. 2. This behaviour in the ion-saturation current measurement already gives us an indication of the position of the PFR and the latter is used as a reference. In case a significant difference between the measurement of the ion-saturation current and the magnetic reconstruction codes is observed, the PFR is adjusted according to the measured ion-saturation current. Lastly, the PFR position determined by the two steps mentioned above, is verified by the plasma parameters determined for the sweeping probe, where a temperature decrease is observed in the PFR region.

The relative fluctuation amplitude of the ion-saturation current is defined as $\tilde{I}^+_\mathrm{sat} = \sigma_{I^+_\mathrm{sat}} / \langle I^+_\mathrm{sat} \rangle$, with $\langle I^+_\mathrm{sat} \rangle$ being the moving mean for a window of 2.4 ms and $\sigma_{I^+_\mathrm{sat}}$ the moving standard deviation for the same time window. The window size is chosen to be a balanced compromise between the statistics and the assumption of the probe head's stationarity. The maximum speed of the probe head is $\approx 3\,\mathrm{ms}^{-1}$. For a pin length of 2 mm, the time taken for the probe head to move the length of the pin is about 0.7 ms. However, a window of 0.7 ms consists of merely 350 data points. In order to have sufficient statistics we, therefore, consider the probe head to be quasi-stationary in the window of 2.4 ms.

With the sweeping Langmuir probe pin, I-V characteristics are collected along the XPM trajectory. Using a standard fitting method [25], the following plasma parameters can be extracted: floating potential V_float, effective ion-saturation current $I_\mathrm{sat,eff}$, and electron temperature T_e. The local electron density profile n_e, and the plasma potential V_plasma are given as follows: $n_\mathrm{e} = \frac{I_\mathrm{sat,eff}}{A\,e}\left(\frac{m_\mathrm{i}}{2T_\mathrm{e}}\right)^{1/2}$ and $V_\mathrm{plasma} = V_\mathrm{float} + \gamma T_\mathrm{e}$, where A is the exposed area of the Langmuir probe pin and m_i is the ion mass. For He-4 and D

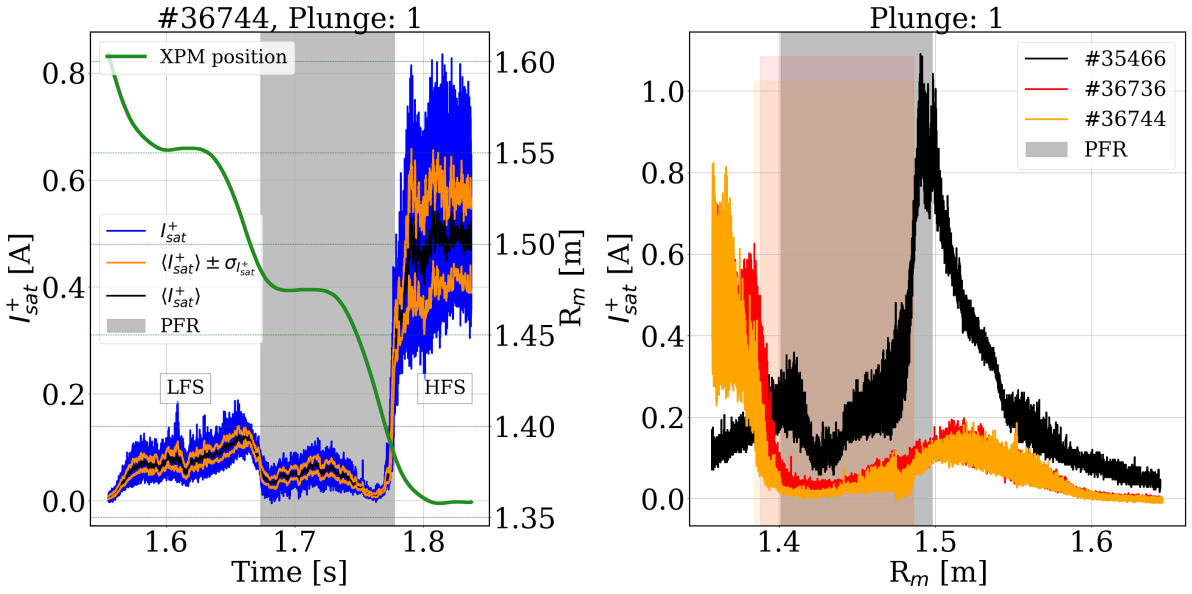

(a) (b)

Figure 2: (a) The I^+_{sat} measured by the biased Langmuir probe pin 1 during the insertion phase of the first plunge. The XPM trajectory is represented by the green line. Figure taken from [22]. (b) The analysis domain of I^+_{sat} of the first plunge of the three discharges are shown as a function of major radius R_m. The PFR for the corresponding plunges is shown by the colored shaded region. Please refer to the digital version for the color coding.

plasma, γ is calculated to be approximately 3.2 and 2.8, respectively [25]. Since the electron-saturation branch is usually not measured in strongly magnetized plasma, cut-off values in the voltage and current ranges are determined to optimize the curve fitting. Fig. 3 (a) shows an example of an I-V curve and the plasma parameters determined from fitting. Here, the cut-off values in the voltage and current range were +50 V and -1.0 A, respectively. Fig. 3 (b) shows the coefficient of determination R^2 as a function of the major radius R_m with the blue line representing the position of the I-V characteristics in Fig. 3 (a). It is seen that the plasma parameters determined are able to describe the I-V characteristics well with a $R^2 > 0.94$. The slight decrease in the R^2 values is due to the scattering points at the large sweeping voltage, which have been considered during the comparison between the predicting model (see [25]) with the I-V characteristics.

Since the Langmuirs pins are cylindrical and the region of measurements is dominated mostly by toroidal magnetic field, it is assumed that the magnetic field are perpendicular to the Langmuir pins. Therefore, a thin sheath is approximation is made. To validate the plausibility of the assumptions, the plasma parameters determined for using the XPM diagnostics is compared with those determined by Langmuir probes embedded in the divertor of ASDEX Upgrade and the results is shown in Fig. 4 for the LFS SOL. Fig. 4 shows the electron temperature, the floating potential and the electron

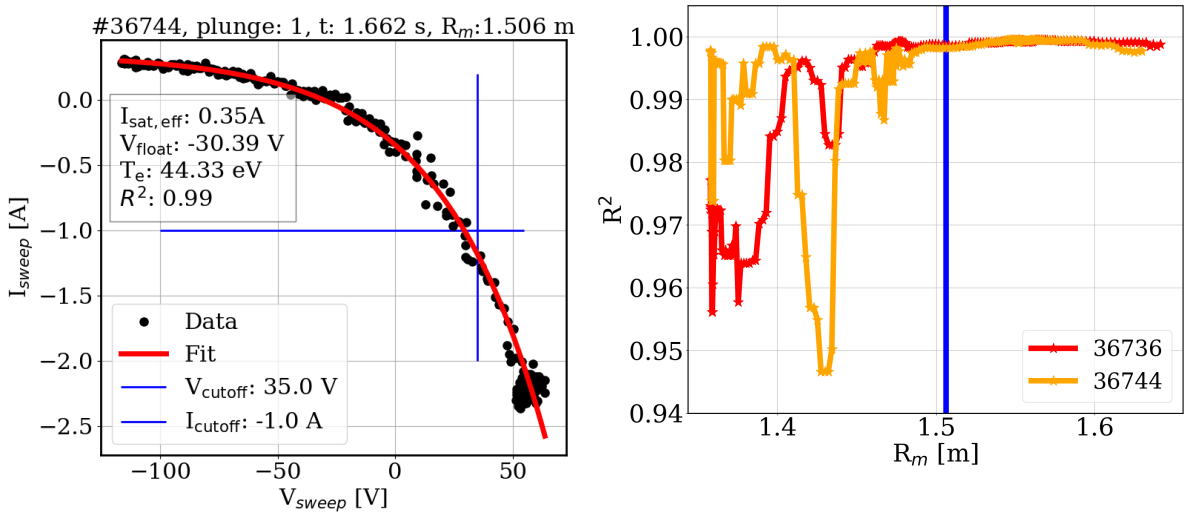

(a) (b)

Figure 3: (a) Example of an I-V curve (obtained at $R_m = 1.506$ m (see Fig. 5 (b) with $V_{\text{plasma}} = 133$ V and $n_e = 0.5 \times 10^{19}\text{m}^{-3}$) during the first plunge in the He plasma #36744) and the corresponding plasma parameters, (b) the coefficient of determination R^2 for each I-V curves. Figures taken from [22]

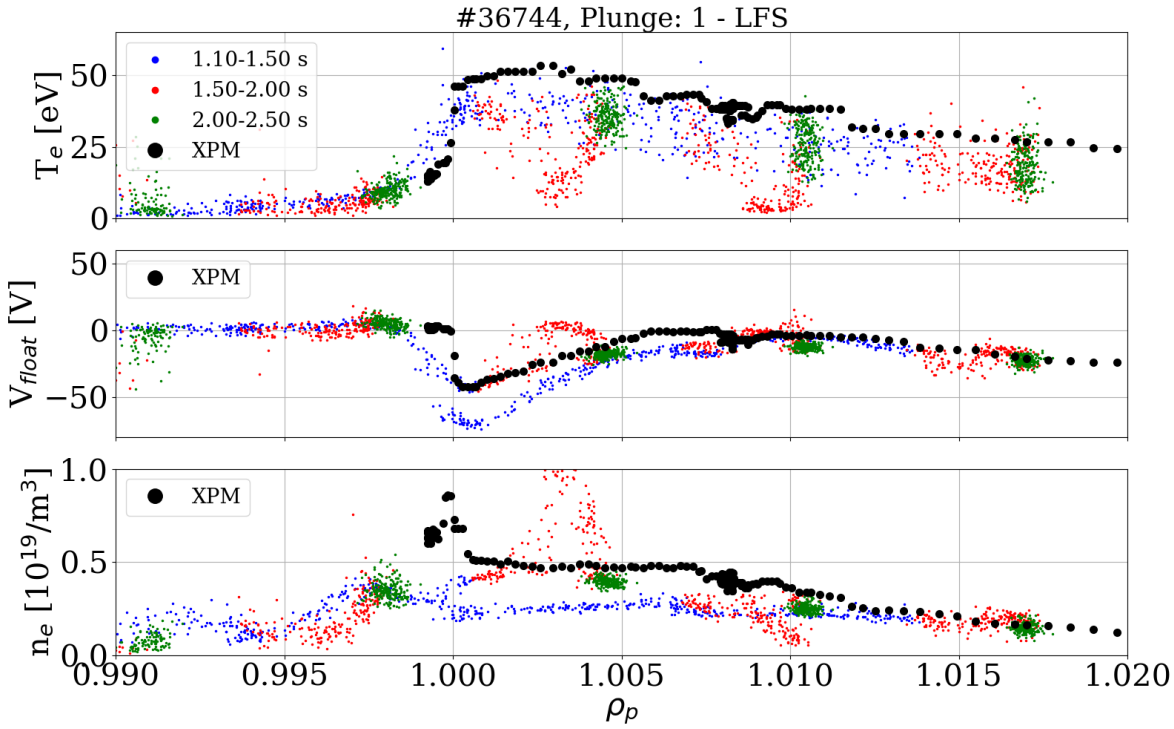

Figure 4: Comparison of the determined plasma parameters using the XPM mounted sweeping Langmuir pin with the divertor-embedded Langmuir probes as a function of the poloidal flux surface label ρ_p for the LFS SOL. Figure taken from [22].

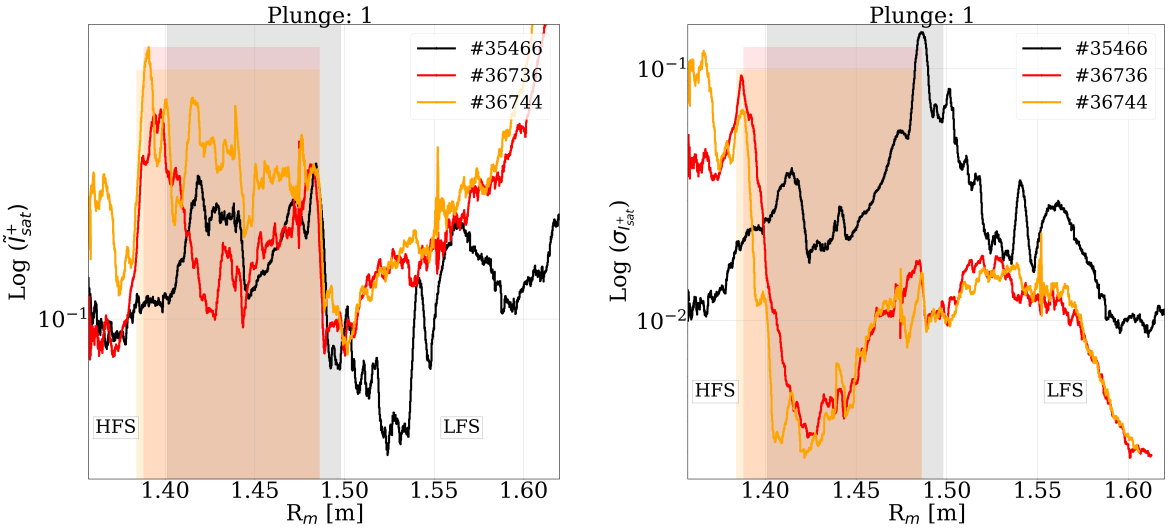

Figure 5: (a) The logarithmic relative fluctuation amplitude, Log($\tilde{I}^+_{\rm sat}$), and (b) The logarithmic absolute fluctuation amplitude Log($\sigma_{I^+_{\rm sat}}$) of the first plunge. Both fluctuation amplitudes are given as a function of the major radius R_m.

density as a function of the poloidal flux surface label ρ_p. The plasma parameters are determined for the three time intervals: 1.1 - 1.5 s (before XPM plunge, in blue), 1.5 - 2.0 s (during XPM plunge, in red) and 2.0 - 2.5 s (after XPM plunge, in green). The plasma parameters determined by the XPM-Langmuir pin are shown as black circles and a good agreement is observed with the divertor Langmuir probes just before and after the XPM plunge. During the XPM plunge, the probe itself disturbs the plasma in the divertor region. This results in scattering data points during the plunge interval (see data points in red colour in Fig. 4) and therefore, cannot be compared directly. However, the good agreement of the plasma parameters before and after the plunge shows that in a sheath regime the thin-sheath approximation in the X-point region is valid.

4. Results

The relative fluctuation and the absolute fluctuation amplitude of the ion-saturation current as a function of the major radius R_m are shown in Fig. 5 in a semi-logarithmic scale.The probe head trajectory spans from the LFS (**large** R_m values) to the HFS (**small** R_m values). From the far SOL towards the LFS separatrix leg, a decreasing trend is observed in the relative fluctuation level, while a decrease in the absolute fluctuation level is observed close to the separatrix leg on the LFS SOL. When entering the PFR the relative fluctuation level increases significantly. In fact, the lowest relative fluctuation level in the plasmas is reached at the LFS separatrix leg, providing a clear indication for the presence of a quiescent region just before the PFR. It should be noted that

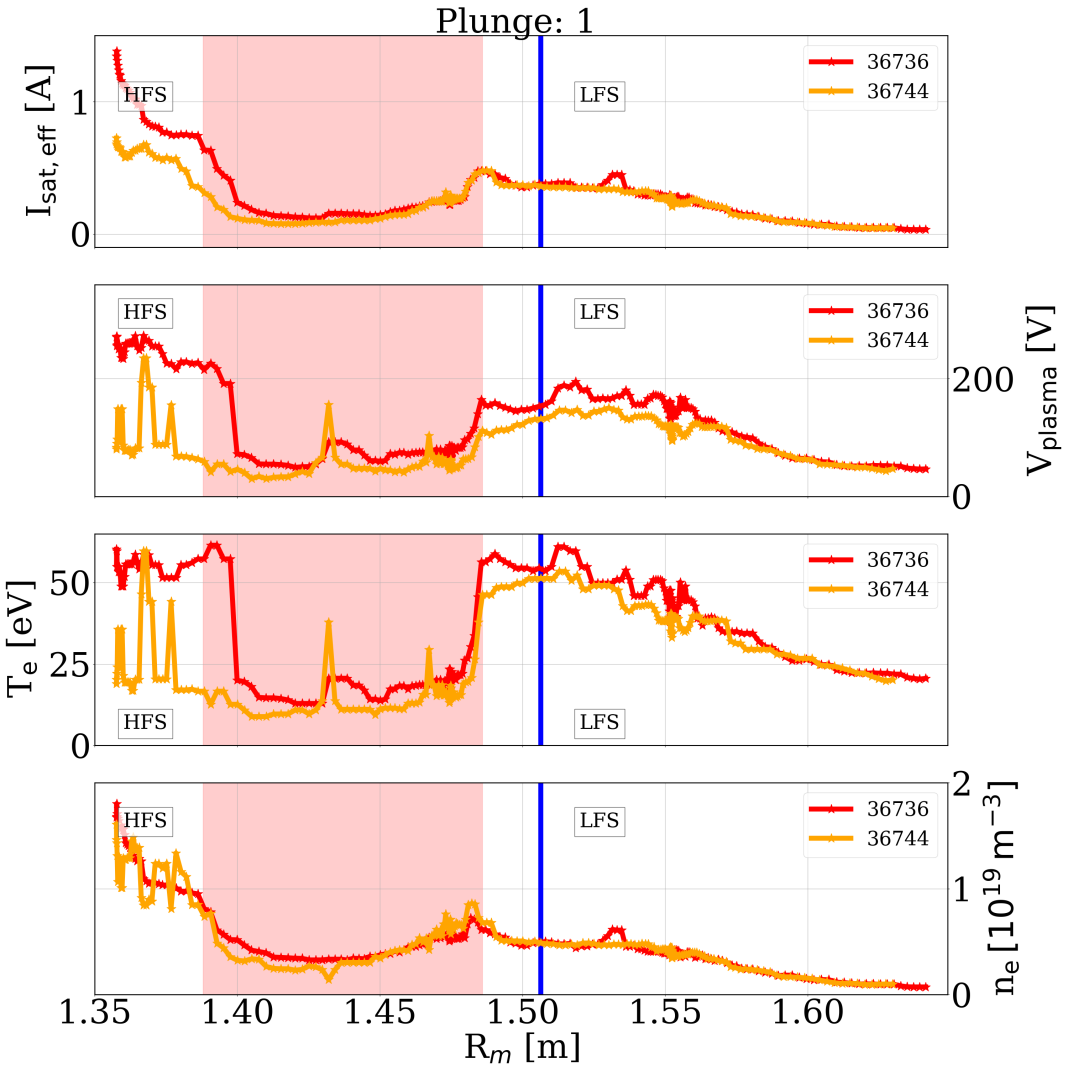

Figure 6: The profile of the plasma parameters from the swept Langmuir pin for the He plasmas (#36736 and #36744). There was no sweeping pin during the D discharge #35466. The shaded regions represent the PFR of each discharge and are in the same color-coding. The blue line represents the parameters of the I-V curve shown in Fig. 3 (a). Figure taken from [22]. Please refer to the digital version for the color coding.

the difference in the trend of the relative fluctuation levels in the LFS SOL between the He and D plasmas might be due to the different divertor conditions. The relative fluctuation levels are elevated in the PFR (coloured shaded region), while the absolute fluctuation level decreases in the PFR. This is also observed in the second and third plunges of all three discharges. Fig. 6 shows the plasma parameters as a function of the major radius R_m and it indicates that the elevated fluctuation level is followed by a drop in both temperature and density. A steep temperature drop is observed in the PFR, but the density drop is not as significant as the temperature drop. The temperature drops by approximately 60% while the density changes by approximately 30%.

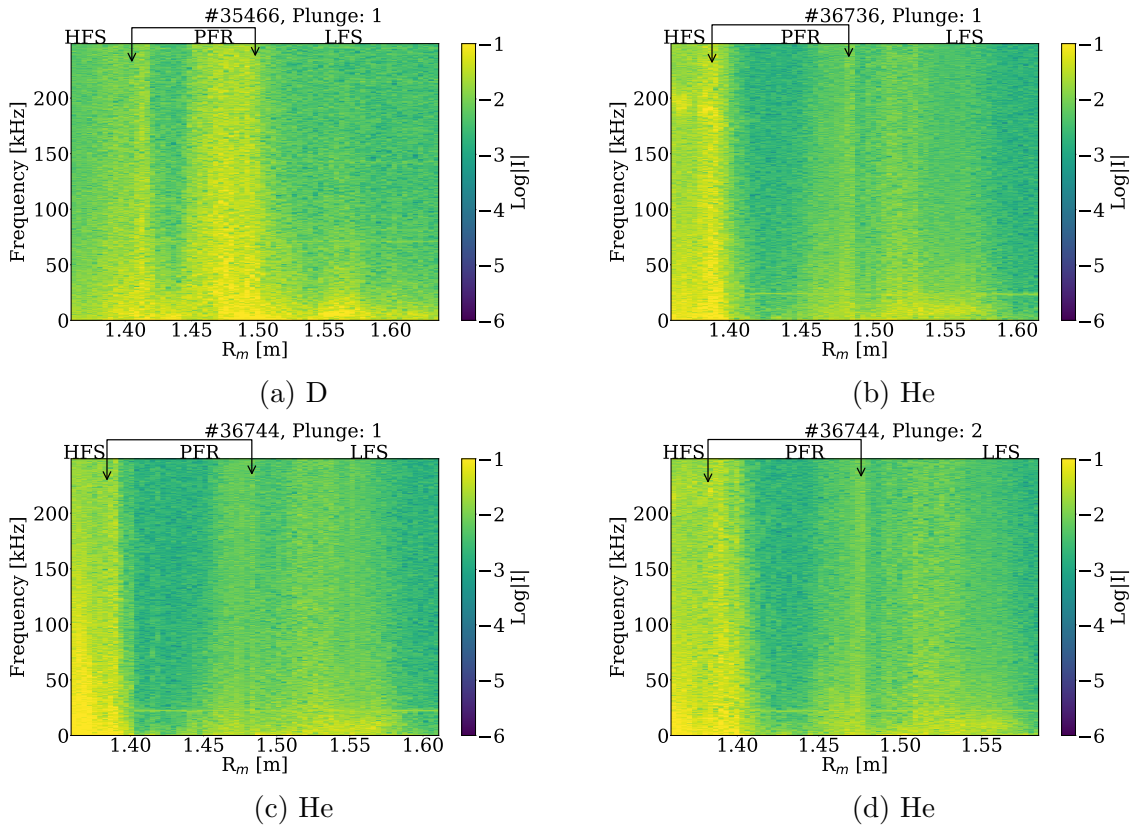

(a) D (b) He

(c) He (d) He

Figure 7: Spectrogram of I_{sat}^{+} of the first plunges of discharge #35466 (a), #36736 (b) and #36744 (c), respectively, and the second plunge of discharge #36744 (d). The color scale gives the amplitude I of the Fourier transform in the logarithmic scale. The private flux region is located between the arrows. Figures taken from [22].

In the HFS SOL, the relative fluctuation level of the NBI heated plasmas (#36744) is double of that of the ECRH plasmas (#35466, #36736). This pronounced difference is also reflected in the plasma parameters and, in general, in the ion-saturation current profiles. A reason for this discrepancy could be the detachment of the inner divertor target. However, analysis of data from Langmuir probes embedded in the ASDEX Upgrade divertor did not show any clear detached divertor profiles. Thus, the reason for large difference in fluctuation between the two heating schemes influencing only the HFS conditions would need further dedicated investigations.

4.1. Spectral Analysis

A spectral analysis is performed on the ion-saturation current with the results presented in Fig. 7. The amplitude, I, on the HFS for the He plasmas (for $R_m < 1.40$ m for both plunge 1 and 2) is larger compared to that in the LFS SOL and PFR. A similar trend is observed for the density (see Fig. 2 and note that $n_{\mathrm{e}} \propto I_{\mathrm{sat}}^{+}$), where we see that the ion-saturation current measured in the HFS SOL is larger compared to the LFS SOL for the He plasmas. For the D plasma, the amplitude is smaller on the HFS SOL compared

to the He plasmas. This is due to the low ion-saturation current measured on the HFS SOL during the D plasma.

In general, we also observe an increase in the fluctuation level close to the inner separatrix leg on the HFS. The large fluctuation amplitudes could be interchange-driven turbulence as the pressure gradient and magnetic curvature vector are anti parallel in this region.

Interestingly, two bands with low fluctuation amplitudes are observed in all discharges. Both of these bands extend to almost the entire frequency range. Note that the quiescent regions in this work is defined as the regions of low fluctuations. The first band appears right before the PFR (i.e before crossing the LFS separatrix) and the second band, which is more pronounced, appears in the HFS PFR. In the He plasma (#36744), the first band is more visible in Fig. 7 (d) compared to Fig. 7 (c). The two bands are observed for all plunges made during the three discharges. It should be noted that the turbulence appears rather broadband. A mode appearing on the HFS around 200 kHz in Fig. 7 (b) is observed and it has been identified to be a toroidicity-induced Alfvén eigen mode, which as a core mode is beyond the scope of the presented investigation.

The first band shows the presence of the quiescent region observed in Fig. 5 (a), whereas the second band indicates yet another quiescent region located in the PFR. We defer the discussion of this region of low fluctuation to section 5.

Since the observed quiescent regions extend to the entire explored frequency range, we integrate the amplitude of the fluctuations over all frequencies to make them more visible, i.e., $\log(\int_f \mathrm{I}\,\mathrm{d}f)$. Figure 8 shows the profiles of the integrated amplitudes for both the first and the second plunge, where both regions of low fluctuations are now clearly visible. It is observed that the behaviour of the integrated amplitudes in Figure 8 (a) resembles that of the absolute fluctuation level in fig. 5 (b), which is given in a semi-logarithmic scale. Thus, showing the consistency of the presented measurements.

The drop in amplitude close to the LFS separatrix leg (right arrows in Fig. 8) supports the presence of a quiescent region as also observed in other tokamaks [12–15]. The second drop in amplitude in the HFS PFR (left arrows in Fig. 8) supports yet another quiescent region, which has, to the authors' knowledge, not been reported before.

5. Discussion and Conclusion

The X-point manipulator at ASDEX Upgrade gives the unique possibility of an increased poloidal diagnostic coverage in the X-point region. Using a Langmuir probe, the ion-saturation current has been measured from the LFS to the HFS via the PFR. On the LFS, the relative fluctuation level decreases before the separatrix leg is crossed (see Fig. 5 (a)), giving the first indication of a region of low fluctuations in ASDEX Upgrade. This first quiescent region (indicated by orange box 'I' in Fig. 9) is most likely caused by the strong magnetic shearing around the X-point. This is consistent with the experimental

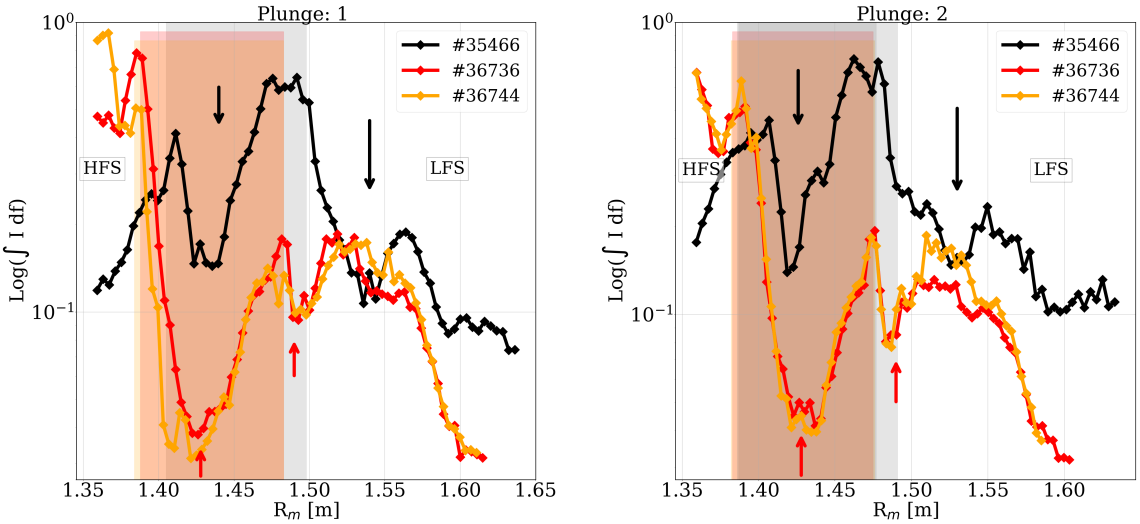

(a) (b)

Figure 8: The integrated amplitude I as a function of major radius R_m during (a) the first plunge and (b) during the second plunge of discharges #35466, #36736, and #36744. The PFR is marked by the shaded areas. Figures taken from [22].

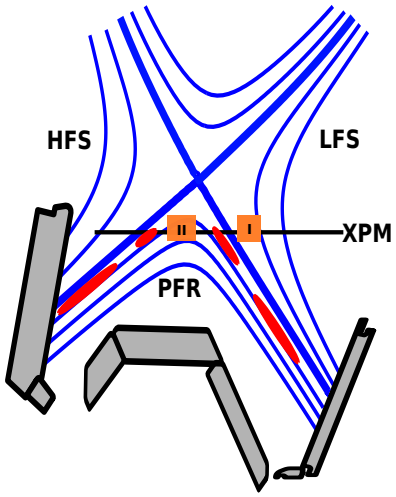

Figure 9: Schematics of the approximate position of the two quiescent regions in the poloidal cross-section of ASDEX Upgrade's divertor region. The magnetic field lines are represented in blue and the XPM trajectory is shown by the black line. Filaments that are generated in the HFS separatrix leg and propagating radially towards the LFS are coloured in red. The approximate position of the *two* quiescent regions are illustrated by the orange boxes and are marked by 'I' and 'II'. Figure taken from [22].

observations from MAST [12], NSTX [14, 15] and TCV [13], as well as with simulation

results [16–18]. Tanaka et al. [26] also reported a decreasing relative fluctuation level near the separatrix. The increase of relative fluctuation in the LFS PFR (Fig. 5 (a), shaded region) is consistent with the observations made at JET by García-Cortés et al. [27]. They performed a strike point sweep of 4 Hz at the divertor targets to allow the measurements of fluctuation profiles in the SOL and PFR using Langmuir probes embedded in the divertor targets at JET. They reported an elevated relative fluctuation level in the PFR compared to the LFS SOL.

Furthermore, a decrease in the fluctuation amplitude close to the HFS separatrix leg (1.40 m $< R_m <$ 1.45 m) has been identified by means of spectral analysis (see Fig. 7 and 8). This supports the existence of a quiescent region located in the PFR (indicated by orange box 'II' in Fig. 9). However, the underlying mechanism for the existence of the second quiescent region in the PFR seems to be different from the first one observed in the LFS SOL. We observe a decrease in the absolute fluctuation amplitude in the PFR (Fig. 5 (b) and Fig. 8(a)) at $R_m \approx 1.42$ m whereas at this position in Fig. 5 (a), the relative fluctuation levels are elevated, especially for discharges #35466 and #36744. The difference between the relative fluctuation level and the spectral analysis, gives an indication that the regions of low fluctuations in the HFS PFR and the LFS SOL might be due to two different mechanisms.

Before crossing the HFS separatrix leg, the amplitude of the fluctuations increases again (Fig. 7 and 8), indicating a turbulent HFS PFR at ASDEX Upgrade. Harisson et al. [28,29] reported a turbulent PFR on the HFS in MAST, where primary filaments are created on the inner separatrix leg and eject secondary filaments deeper into the PFR. A damping of filaments in the HFS PFR was observed by simulation [16] and has been related to an inefficient turbulent transport of filaments towards the PFR. The exact nature of the second quiescent region is unknown. However, a possible explanation is illustrated in Fig. 9. There is no source of instability in the center of the PFR as the gradients are relatively flat. Turbulence in this region, therefore has to be generated somewhere else and propagate into this region. In the PFR, the pressure gradients are only steep close to the separatrix legs. It is therefore, expected that filaments in the PFR are created in the region of bad curvature close to the inner separatrix leg on the HFS by the interchange instability as proposed in [28, 29]. Also Kelvin-Helmholtz instabilities may be excited across the inner separatrix leg due to sheared E×B flows generated by the electron temperature gradient at the inner divertor target and the inner divertor leg maybe also subject to the divertor leg instability [30–32], which is driven by the electron temperature gradient at the target as well. The filaments generated at the inner separatrix leg mainly propagate parallel to the magnetic field lines towards the inner and the outer divertor target. Therefore, they stay close to the separatrix leg. The filaments propagating from the inner leg to the outer divertor target are seen at the height of the X-point manipulator on the left hand side of region 'II'. Primary filaments propagating close the X-point are likely shredded here. These might lead to secondary smaller filaments propagating to the outer leg generating the turbulence between region 'I' and 'II' or the turbulence in the PFR at the outer divertor leg is driven locally by

Kelvin-Helmholtz or the divertor leg instability. It is also likely that the filaments do not propagate far enough into the PFR, thus resulting in a low turbulence, i.e., a quiescent region. For the identification of the possible different instabilities, measurements of different fields (e.g., potential, density and electron temperature) will be necessary.

To summarize, from the experiments carried out at ASDEX Upgrade, two quiescent regions are observed in both deuterium and helium plasmas. The formation of the quiescent regions is found to exist in both helium and deuterium plasmas and is independent of the heating source. It therefore, seems likely that it is a consequence of the magnetic configuration and thus, its formation should be independent of the heating source and plasma ion type. However, the different behaviour of the relative fluctuation level and that of the absolute fluctuation level indicates that the formation of the two region of low fluctuations are due to different mechanism. It is also possible that the quiescent region extends on the magnetic flux surfaces in the PFR and should be investigated with more experimental data. Further experiments are planned to scan the PFR at different positions below the X-point, i.e., in the poloidal direction. This might indicate if there exists any correlation between the magnetic shearing around the X-point and the formation of the second quiescent region in the private flux region. Finally, it could be interesting to investigate whether the formation of the quiescent regions has an effect on the power deposition on the PFCs. To investigate the mechanism behind the existence of the quiescent region in the HFS PFR, calls for more experimental data. Due to the lack of experimental data around the X-point, we aim to contribute in improving the literature and further understanding of the divertor physics.

Acknowledgments

This work has been carried out within the framework of the EUROfusion Consortium and has received funding from the Euratom research and training programme 2014-2018 and 2019-2020 under grant agreement No 633053. The views and opinions expressed herein do not necessarily reflect those of the European Commission. We would like to thank D. Brida, M. Wiesenberger, L. Gil and A. H. Nielsen for their fruitful discussions.

References

[1] V. Naulin, *Turbulent transport and the plasma edge*, 2007 J. Nucl. Mater. 363-365 24-31
[2] O.E. Garcia, *Turbulent transport in the TCV SOL*, 2007 J. Nucl. Mater. 363-365 575
[3] O.E. Garcia et al., *Interchange turbulence in the TCV scrape-off layer*, 2006 Plasma Phys. Control. Fus. 48, L1
[4] D. Carralero et al., *An experimental investigation of the large density transition of the scrape-off layer transport in ASDEX Upgrade*, 2014 Nucl. Fusion 54 123005
[5] N. Vianello et al., *Scrape-off layer transport and filament characteristics in high-density tokamak regimes*, 2019 Nucl. Fusion 60 016001
[6] D. Carralero et al., *Experimental Validation of a Filament Transport Model in Turbulent Magnetized Plasmas*, 2015 Phys. Rev. Letter 115 215002
[7] P.C. Stangeby et al., *Plasma boundary phenomena in tokamaks*, 1990 Nucl. Fusion 30 1225

[8] D. Farina et al., *Effect of the magnetic field geometry on the flute-like perturbations near the divertor X point*, 1993 Nucl. Fusion 33 1315-1317
[9] M.V. Umansky et al., *Simulation of turbulence in the divertor region of tokamak edge plasma*, 2005 J. of Nucl. Mater. 337-339 266–270
[10] R.J. Maqueda et al., *Edge turbulence measurements in NSTX by gas puff imaging*, 2001 Rev. Sci. Instrum. 72 931
[11] Terry J.L. et al., *Observations of the turbulence in the scrape-off-layer of Alcator C-Mod and comparisons with simulation*, 2003 Phys. Plasmas 10 1739
[12] N.R. Walkden et al., *Quiescence near the X-point of MAST measured by high speed visible imaging*, 2017 Nucl. Fusion 57 126028
[13] N.R. Walkden et al., *Fluctuation characteristics of the TCV snowflake divertor measured with high speed visible imaging*, 2018 Plasma Phys. Control. Fusion 60 115008
[14] F. Scotti et al., *Divertor leg filaments in NSTX-U*, 2018 Nucl. Fusion 58 126028
[15] F. Scotti et al., *Disconnection of scrape off layer turbulence between the outer midplane and divertor target plate in NSTX*, 2020 Nucl. Fusion 60 026004
[16] D. Galassi et al., *Drive of parallel flows by turbulence and large-scale E×B transverse transport in divertor geometry*, 2017 Nucl. Fusion 57 036029
[17] D. Galassi et al., *Tokamak Edge Plasma Turbulence Interaction with Magnetic X-Point in 3D Global Simulations*, 2019 Fluids 4, 50
[18] F. Nespoli et al., *3D structure and dynamics of filaments in turbulence simulations of WEST diverted plasmas*, 2019 Nucl. Fusion 59 096006
[19] M. Tsalas et al., *Langmuir probe measurements in the lower x-point vicinity of the ASDEX Upgrade divertor*, 2005 J. of Nucl. Mater. 337-339 751-755
[20] M. Tsalas et al., *Divertor plasma flow near the lower x-point in ASDEX Upgrade*, 2007 Plasma Phys. control. Fusion 49 857-872
[21] S. H. Mueller et al., *Direct observations of L-I-H and H-I-L transitions with the X-point reciprocating probe in ASDEX Upgrade*, 2014 Phys. Plasmas 21 042301
[22] R. D. Nem, *Probe Measurements in the X-point Region at ASDEX Upgrade*, 2020 Ph.D. thesis at Technical university of Denmark
[23] R. Fischer et al., *Coupling of the flux diffusion equation with the equilibrium reconstruction at ASDEX Upgrade*, 2016, Fusion Sci. and Technol. 69 526-536.
[24] P. J. McCarthy et al., *The CLISTE interpretive equilibrium code*, 1999 IPP-5/85 International Nuclear Information System No. 31057068 Vol 31
[25] J. Wesson, *Tokamaks*, Clarendon-press-Oxford 2004 3rd edition, section 9.2 and 10.9
[26] H. Tanaka et al., *Statistical analysis of fluctuation characteristics at high- and low-field sides in L-mode SOL plasmas of JT-60U*, 2009 Nucl. Fusion 49 065017
[27] I. García-Cortés et al., *Characterization of fluctuations in the JET Divertor plasmas with Langmuir probes*, 1996 Plasma Phys. Control. Fusion 2051-2062 38
[28] J. R. Harisson et al., *Filamentary transport in the private flux region in MAST*, 2015 J. of Nucl. Mater. 463 757-760
[29] J. R. Harisson et al., *The appearance and propagation of filaments in the private flux region in Mega Amp Spherical Tokamak*, 2015 Phys. Plasmas 22 092508 205002
[30] D. D. Ryutov et al., *Instability driven by sheath boundary conditions and limited to divertor legs*, 2004, Contrib. Plasma Phys. 44, 168-175, No. 1-3
[31] R. H. Cohen et al., *Theory and fluid simulations of boundary-plasma fluctuations*, 2007 Nucl. Fusion 47, 612-625, 7
[32] D. D. Ryutov et al., *Geometrical effects in plasma stability and dynamics of coherent structures in the divertor*, 2008 Contrib. Plasma Phys. 48, 78-57, No. 1-3